SURFACE CURVATURE INFLUENCE ON FLOWFIELD STRUCTURE IN A MICRONOZZLE ARRAY

Israel B. Sebastião, israel@lcp.inpe.br
Wilson F. N. Santos, wilson@lcp.inpe.br
Combustion and Propulsion Laboratory (LCP), National Institute for Space Research (INPE), Cachoeira Paulista-SP, 12630-000

Abstract. *A numerical simulation of a rarefied flow in a convergent-divergent micronozzle, with rectangular cross-section, is performed in the present work. Such a device is considered as part of a micronozzle array. The inlet and outlet boundary conditions are based on pre-defined values of pressure. In general, the performance of propulsive systems is highly dependent on the aerodynamic design of the divergent nozzle portion. In this context, for a defined area ratio, the influence of different divergent shapes on the flowfield structure is investigated by employing the Direct Simulation Monte Carlo (DSMC) method. The computational results obtained pointed out the sensitivity of the primary properties to changes on the divergent shape. It was found that the radius of curvature of the divergent surface performs a small influence on the present micronozzle flowfield.*

Keywords: *DSMC, Rarefied Flow, MEMS, Micronozzle*

1. INTRODUCTION

The recent tendency in the design of space systems has aligned to reduce the life cycle cost of space programs by means of a reduction in the complexity of satellite missions (Konecny, 2004). In this context, one of the possible options concerns to the reduction in the mass of the whole system. The mass reduction will be possible only with a system miniaturization, i.e., a reduction in the satellite scale or in part of it. In this way, concepts of micropropulsion based on microtechnologies have been developed in order to attend the requirements of future space missions.

The current state of semiconductor technology based on silicon has allowed the application of silicon plates in the manufacturing process of microscale devices. This manufacturing technique has been applied in the development of small scale systems, called as MEMS (MicroElectroMechanical Systems), and several others microdevices. Among the many MEMS applications are the microunits of low thrust, where micronozzles are present.

Typically, in micronozzle flows, the molecular mean free path λ is of the same order of magnitude of the micronozzle throat size t. In this situation, the overall Knudsen number, $Kn = \lambda/t$, is within the transition flow regime $(0.01 < Kn < 10)$, i.e., between the continuum flow regime and the free molecular flow regime. In such a circumstance, treating the micronozzle flow with a continuum approach may lead to inaccurate results. Consequently, a molecular approach must be employed to describe the micronozzle flow.

According to the current literature, several experimental and numerical studies related to macro- and micronozzles have been performed in order to investigate the influence of certain physical processes on the behavior of such devices. These studies have focused on, among other aspects, the micronozzle performance, Reynolds number influence, effects of 2D versus 3D micronozzle geometries (Alexeenko *et al.*, 2002), behavior of continuum versus high rarefaction regimes, and performance of propulsive systems with micronozzles arranged in array patterns (Horisawa *et al.*, 2009). For the purpose of this brief review, only some relevant studies are described below.

Alexeenko *et al.* (2002) studied numerically the performance of axisymmetric and three-dimensional micronozzles, with rectangular cross-section, by using continuum and kinetic approaches. The simulations showed that the distribution of the macroscopic properties is highly dependent on the flow dimensionality. For the examined conditions, they observed that the surface effects present in the three-dimensional case reduced the thrust level by approximately 5% and 20% in comparison to the axisymmetric and two-dimensional cases, respectively. Therefore, the prediction of three-dimensional micronozzle flows by using a two-dimensional approach may lead to significant errors.

Recently, by using the DSMC method, Horisawa *et al.* (2009) have investigated the behavior of micronozzle flows when they are arranged as singly or as array patterns. Simulations for a single micronozzle showed good agreement with experimental data. In addition, the numerical results for the array arrangement demonstrated a representative increasing of the system performance as well as considerable changes on the structure of the external flow.

According to the relevant literature, the majority of the studies has investigated the micronozzle performance for different length scales and flow conditions. However, these investigations have not focused on the influence of the surface curvature on the micronozzle flow structure. Thus, in order to obtain further insight into the physics of micronozzle flows, a numerical simulation of a rarefied flow in a convergent-divergent micronozzle, with rectangular cross-section, is performed in the present work. In this scenario, the primary goal of this paper is to assess the sensitivity of the macroscopic properties to variations on the radius of curvature of the divergent micronozzle surface. Due to the high rarefaction and nonequilibrium degrees present in microflows, the Direct Simulation Monte Carlo (DSMC) method is employed to simulate the hypersonic two-dimensional flow in a micronozzle array.

2. COMPUTATIONAL TOOL

The DSMC method (Bird, 1994) has become the most common computational technique for modeling complex transitional flows of engineering interest. This method allows to deal with an unlimited range of rarefied flows within regimes that neither Navier-Stokes nor collisionless Boltzmann equations are appropriated. In the past 40 years, the DSMC results have been validated through comparisons with analytical and experimental data in excellent agreement. In spite of the early DSMC applications were performed on hypersonic and high altitude problems, the recent studies on rarefied flows are beyond the aerospace science. Among other applications, one may cite the aforementioned microscale gas flows and the design and processing of materials, e.g., low-pressure simulations on CVD (Chemical Vapor Deposition) and PVD (Physical Vapor Deposition) processes.

In the DSMC method, the gas flow is represented by a large number of simulated particles, where each simulated particle represents a fixed number of real gas particles. The simulated particles are allowed to move, to collide among themselves, and with any boundaries, while the computer stores their position coordinates, velocities and other physical properties such as internal energy. The fundamental assumption employed in the DSMC method is that the movement of the molecules in a dilute gas can be decoupled from the collisions between the molecules if a sufficient small time step is employed. For this reason, the simulation is advanced in time steps that should be less than the mean time between collisions (Bird, 1994).

In the present account, the molecular collisions are modeled by using the variable hard sphere (VHS) molecular model and the no-time counter (NTC) collision sampling technique. The energy exchange between kinetic and internal modes is controlled by the Borgnakke-Larsen statistical model. Simulations are performed using a non-reacting gas model, consisting to 76.3% of N_2 and 23.7% of O_2. Energy exchange between the translational and the internal modes of rotation and vibration are considered. In this connection, relaxation collision numbers of 5 and 50 are used for the calculations of rotation and vibration, respectively.

3. GEOMETRY DEFINITION

As previously mentioned, it is proposed to investigate the influence of geometric aspects of the divergent micronozzle part on the flow structure. The divergent part may be composed by convex and concave surfaces linked by an inflection point. Hence, in this work, different aerodynamic configurations are modeled by changing the curvature of the these surfaces at the inflection point.

The geometry definition is also based on the fact that micronozzles generally have rectangular cross-sections, and they are employed in micronozzle layers or arrays (Horisawa *et al.*, 2009; Zhan *et al.*, 2004). Figure 1(a) presents a typical array pattern of convergent-divergent micronozzles. By focusing on the plane that crosses this array, Fig. 1(b) revels three similar profiles side by side.

Obviously, in order to perform DSMC simulations in this microdevice, a spatial discretization must be applied in the flow region. As reported by Ivanov *et al.* (1999), neglecting the plume region in micronozzle flows, i.e., to simulate only the internal flow, provides over-predicted results. In this sense, a buffer (external) region is included in the present study as depicted in Fig. 1(b). It is clear that such a grid holds a particular symmetry between each nozzle and also along their centerlines. Therefore, it is assumed that the flow study of a micronozzle array can be predicted by simulating only the regions pointed out in Fig. 1(b) with appropriated boundary conditions. Such a simplification yields a tremendous computational saving.

In order to allow a flexible grid to cluster the cells, the flowfield is divided into an arbitrary number of regions, e.g., the nine regions showed in Fig. 2. In this scenario, region 1 represents the inlet chamber, regions 2-3 the convergent part, regions 4-7 the divergent part, and regions 8-9 the buffer zone. Due to the symmetry, dimensions indicated by h means

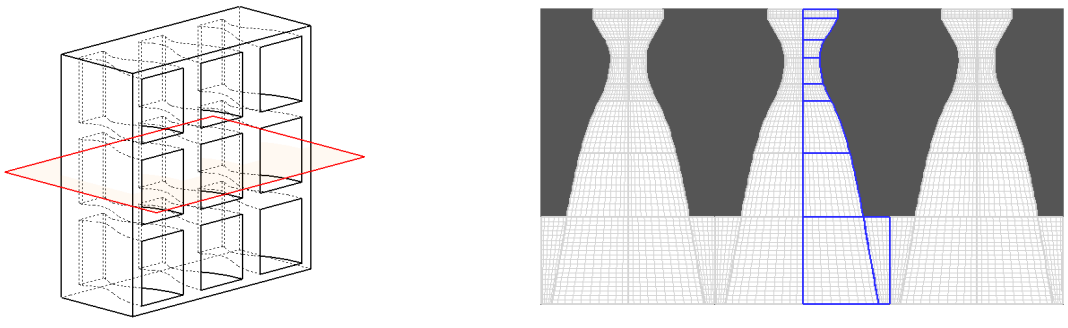

(a) (b)

Figure 1. (a) Isometric view of a micronozzle array and (b) the two-dimensional representation of the simulated regions.

a half size while the lengths are indicated by L. The subscripts in, c, t, d, e and b refer to the inlet, convergent, throat, divergent, exit and buffer sections, respectively.

In this geometry, the convergent part is composed by a surface inclined by a half angle θ_c that is tangent to a round shape of constant radius R_c. In analogous fashion, the convex surface of the divergent part is described by a round shape of constant radius R_d with slope θ_d at the inflection point. On the other hand, the concave surface is described by a power-law shape that depends on a particular exponent n, and constants A and B. As geometric constrains, at the exit section $(x = L_d)$, the concave surface must provide an exit divergent angle θ_e and a half exit size h_e that are pre-defined for all cases. Finally, the buffer zone dimensions, h_b and L_b, are completely independent of the internal micronozzle design.

Based on these arbitrary considerations, the convex $(0 < x \leq L_{d_1})$ and concave $(L_{d_1} < x \leq L_d)$ surfaces in the divergent part can be defined according to Eqs. (1) and (2), respectively. Therefore, y'_{d_1} and y'_{d_2} represent the local slope of each surface, and y''_{d_1} and y''_{d_2} are related to the local radius of curvature.

$$y_{d_1} = h_t + R_d - \left(R_d^2 - x^2\right)^{1/2} \quad (1) \qquad y_{d_2} = A\,(x - B)^n \quad (2)$$

As listed in the following, geometric constrains are applied to express the divergent shape in a mathematical form.

1) In the divergent surface, both the convex and concave functions must be equal at the inflection point;

$$y_{d_1}\,(L_{d_1}) = y_{d_2}\,(L_{d_1}) \quad (3)$$

2) At the inflection point, the ratio between the slope of the concave to the convex surface must be equal to the parameter α_g. Similarly, the absolute value of the ratio between the second derivatives, which are related to the radius of curvature, must be equal to the parameter β_g at the inflection point.

$$\alpha_g = \frac{y'_{d_2}\,(L_{d_1})}{y'_{d_1}\,(L_{d_1})} \quad (4) \qquad \beta_g = \left|\frac{y''_{d_2}\,(L_{d_1})}{y''_{d_1}\,(L_{d_1})}\right| \quad (5)$$

3) At the exit section, the divergent shape must provide a given half size h_e, and the slope of the surface must be equal to a given angle θ_e.

$$y_{d_2}\,(L_d) = h_e \quad (6) \qquad y'_{d_2}\,(L_d) = \tan\theta_e \quad (7)$$

In this stage, for given values of α_g and β_g in addition to the known variables (in black) in Fig. 2, the unknown variables (in red) can be determined by Eqs. (1) to (7). In other words, α_g and β_g are the geometric parameters that control the divergent shape. Moreover, with such a strategy, it is allowed to fix all known variables in Fig.2 and to obtain different geometric configurations by only combining the values of α_g and β_g. By employing the definitions of α_g and β_g, the geometric configurations applied to the present study are listed according to Table 1.

Similarly, Tab. 2 summarizes the arbitrary and common variables used in the geometry definition. These values are somewhat based in previous studies (Alexeenko *et al.*, 2005; Hao *et al.*, 2005) and are normalized by the half throat size h_t that is equal to 10μm. In order to decouple the influence of these variables on the flowfield structure, they are kept with the same value for all simulated cases. The convergent θ_c and the exit divergent θ_e angles are set as 30 and 10 degrees, respectively. In group A cases, both convex and concave surfaces have the same slope at the inflection point $(\alpha_g = 1.0)$, which correspond to a smooth surface transition in the vicinity of the inflection point. Thus, the condition of the radius of curvature is varied by changing β_g.

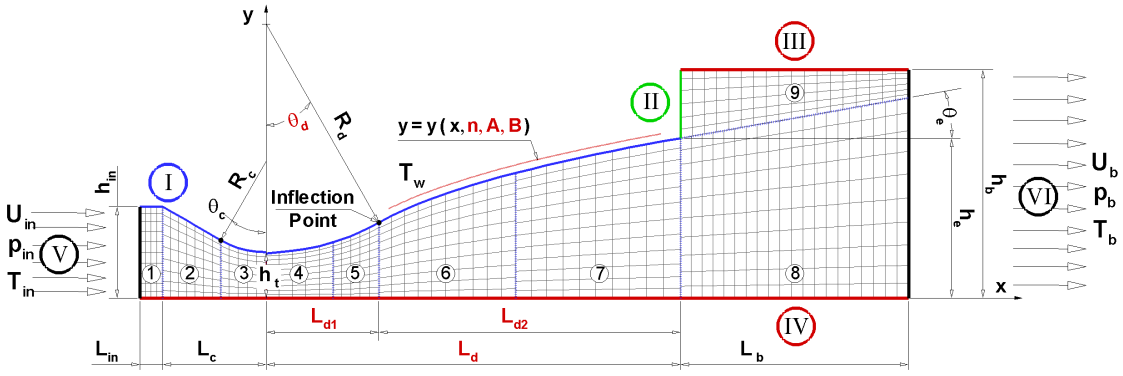

Figure 2. Geometry definition and boundary conditions of the computational domain.

For illustration purpose, Fig. 3 depicts the differences between the geometric configurations defined in Tabs. 1 and 2. In this comparison, for clarity, only the uncommon geometries are shown. Moreover, the region near to the inflection point is zoomed in order to make the meaning of the geometric parameters α_g and β_g more intelligible. In this drawing, the coordinates X and Y represent the lengths x and y normalized by the half throat size h_t, respectively.

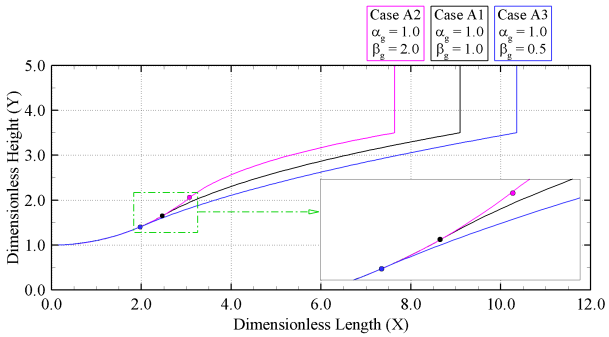

Figure 3. Geometric differences between the cases.

Table 1. Geometric definitions of each case.

Case	α_g	β_g	L_{d_1}/h_t	L_d/h_t	L_{d_1}/L_d	θ_d	n
A1	1.0	1.0	2.47	9.09	0.27	29.6°	0.39
A2	1.0	0.5	3.06	7.64	0.40	37.8°	0.27
A3	1.0	2.0	1.98	10.35	0.19	23.3°	0.51

Table 2. Common geometric definitions.

h_{in}/h_t	h_e/h_t	h_b/h_t	L_{in}/h_t	L_b/h_t	R_c/h_t	R_d/h_t
2.00	3.50	5.00	0.25	5.00	2.00	5.00

Table 3. Flow conditions.

Parameter	**Value**	**Unit**
Inlet pressure (p_{in})	100	kPa
Back pressure (p_b)	5	kPa
Inlet temperature (T_{in})	300	K
Surface temperature (T_w)	300	K
Inlet density (ρ_{in})	1.161	kg/m^3
Inlet number density (n_{in})	2.414×10^{25}	m^{-3}
Inlet viscosity (μ_{in})	1.703×10^{-5}	Pa×s
Inlet mean free path (λ_{in})	5.423×10^{-8}	m
Inlet overall Knudsen (Kn_{in})	0.0027	
Inlet overall Reynolds (Re_{in})	150	

4. COMPUTATIONAL FLOW CONDITIONS

As showed in Figure 2, the convergent part of the micronozzle is simulated in order to reproduce a correct velocity, pressure and temperature distributions in the throat section. Additionally, a buffer zone is introduced to provide a more realistic pressure adjustment and hence to avoid that the downstream boundary conditions perform any influence on the region of interest, i.e., in the divergent part. For cell clustering purpose, the simulated domain is divided into nine regions.

A schematic view of the computational domain is shown in Figure 2. According to this figure, the simulated domain is composed by six boundary types. The boundaries I and II represent the internal and external surfaces of the micronozzle, respectively. Diffuse reflection is the physical treatment applied for each molecule that interacts with these surfaces. Due to the aforementioned symmetry assumptions, the boundaries III and IV are treated as symmetry planes, where there is no normal gradients. The sides V and VI represent the upstream and downstream inflow boundaries. As an initial condition, the inlet velocity u_{in} is predicted analytically by assuming an one-dimensional, steady and isentropic compressible flow. This value is determined in a such manner that sonic conditions are obtained in the throat region. Both the upstream and downstream boundary conditions are described in terms of pre-defined pressures (Wang and Li, 2004).

Based on Figure 2, the main geometric and physical parameters can be summarized by the expansion area ratio h_t/h_e, the exit divergent angle θ_e, the surface temperature T_w, the back pressure (buffer) p_b, and the pressure p_{in} and temperature T_{in} in the inlet boundary.

The present study focused on the geometric influence of the divergent part on the flow structure. As listed in Table 1, this effect is studied by simulating different geometric configurations at the inflection point. The flow conditions employed are somewhat based on values that are commonly observed in practical applications and numerical simulations for cold gas propulsive systems (Alexeenko *et al.*, 2002; Hao *et al.*, 2005). For the three investigated cases, the flow is choked at the throat.

The working fluid properties considered in this study are the same as those found in pertinent literatures (Bird, 1994). In this sense, Table 3 presents the main properties of the inlet gas flow as well as the flow conditions of the external environment (buffer). The inlet pressure p_{in} is assumed to be equal to 100 kPa and the back pressure p_b equal to 5 kPa, which correspond to an expansion pressure ratio p_{in}/p_b equal to 20. The inlet gas temperature T_{in} and wall temperature T_w are equal to 300 K.

By assuming the throat size $(2 \times h_t)$ as the characteristic dimension and taking the inlet mean free path λ_{in}, the overall Knudsen Kn_{in} and Reynolds Re_{in} numbers are approximately equal to 0.0027 and 150, respectively. It is worthwhile to observe that the thermodynamic properties changes along the micronozzle. Then, for an overall Knudsen number based on the throat size and back pressure, the Kn value is about 20 times greater than that one based on the inlet conditions.

Such a wide range of Knudsen values in addition to possible regions in thermal nonequilibrium justify the molecular approach employed in the present study.

The numerical accuracy in the DSMC method depends on the cell size, on the number of particles per computational cell as well as on the time step chosen. These effects were investigated in order to determine the number of cells and the number of particles required to achieve grid independence solutions. Grid independence was tested by running, independently, the calculations with half and double the number of cells in x and y directions compared to a standard grid. Similar investigations were applied to the time discretization. In addition, the present account employed around 1,200,000 simulated molecules. This value demonstrated to be sufficiently large to make statistical correlations between the molecules insignificant. Such analysis (not shown) indicated that the number of simulated molecules, time step and grids used provide solutions fully grid independent.

5. COMPUTATIONAL RESULTS AND DISCUSSION

Since the present simulations were carried out over a wide range of conditions and properties, it proves worthwhile to summarize the main features of the results. In this connection, the purpose of this section is to discuss and to compare influences on the primary properties due to variations on the radius of curvature of the divergent surface. For the present account, the properties of particular interest are velocity, expressed in terms of the Mach number, pressure and temperature.

5.1 Mach Field

Mach number M profiles along the micronozzle and their dependence on different divergent shapes are illustrated in Fig. 4. These profiles are presented for three different cross-sections between the throat and exit. In this set of pictures, X_{Ld} stands for the x-coordinate normalized by the length of the divergent region L_d and Y refers to the y-coordinate normalized by the half throat size h_t. Therefore, for all cases, X_{Ld} equal to 0.0 and 1.0 represent throat and exit cross-sections, respectively.

By looking to Fig. 4, it is seen that for the three sections the Mach distribution is essentially uniform in the centerline $(Y = 0.0)$ vicinity. On the other hand, due to the viscous effects, these profiles demonstrate small, but nonzero, values of M near to the surface. Since in a such vicinity the stream velocity is parallel to the surface, it is reasonable to interpret these nonzero Mach numbers as an indication of a velocity slip. Such phenomenon is a classical feature in rarefied flows. By comparing the throat and exit sections, it is clearly observed that this velocity slip increases in the downstream direction. Near to the nozzle lip, the flow acceleration and wall heat transfer reduce the local density. As a result, rarefaction and nonequilibrium degree increase and then the velocity slip becomes more significant.

As expected, the Mach number increases downstream along the x-direction with the cross-section area rise. Based on the isentropic quasi-one-dimensional continuum approach, for the present geometry, the centerline Mach number should be equal to 2.8 at the exit section. In contrast, the profiles show Mach values smaller than 2.8 at $X_{Ld} = 1.0$ and $Y = 0.0$. A possible reason for such results is the presence of irreversible processes – friction and heating – in the real flow. In the present profiles, the ratio between the Y range where the Mach distribution is nonuniform to the total Y range of a particular profile is an indication of the viscous layer influence. In general, the results show that such a ratio increases downstream along the x-direction. Therefore, the thickness of the viscous layer increases along the divergent region.

Another important aspect is related to the Mach number distribution at the throat. According to the isentropic quasi-one-dimensional assumption the flow properties are uniform along the entire cross section and vary only in the flow direction. In such approach, the first sonic point, i.e., $M = 1.0$, is at the throat. In contrast, Fig. 4 demonstrates a subsonic condition at $X_{Ld} = 0.0$. This different result is assigned to the fact that for microscale flows, which present high surface-

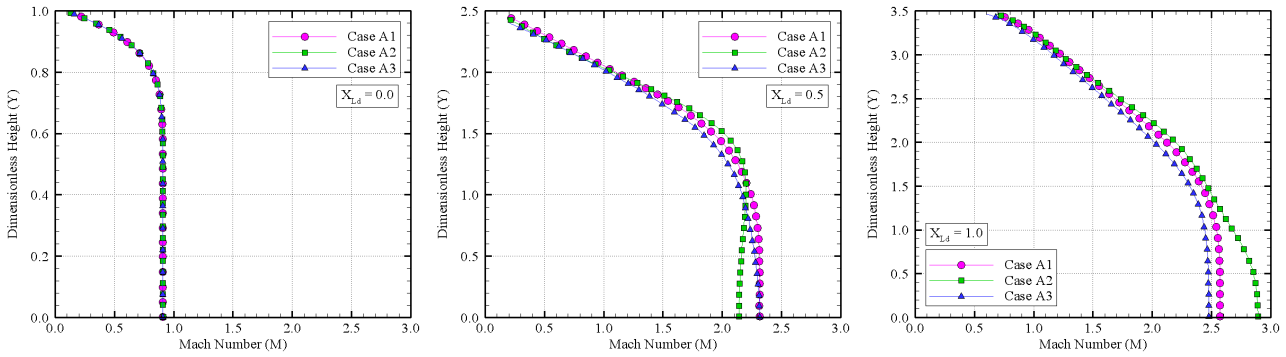

Figure 4. Mach number (M) profiles along the micronozzle for group A cases.

to-volume S/V ratio, the viscous layer thickness is comparable to the cross-section height or depth. Basically, within such layer the distribution of the properties is nonuniform and irreversible processes, e.g., viscous dissipation, are intense. As a consequence, for the same boundary conditions, the quasi-one-dimensional and isentropic assumptions breakdown with decreasing the flow scale. As indeed it is clear from Fig. 4, no significant influence is observed in the local Mach number profiles by changing the radius of curvature for the range of β_g investigated in this work.

At this point, it is worthwhile to take an overview on the streamline traces in the micronozzle. In this manner, Fig. 5(a) illustrates the streamlines for case A1. An interesting characteristic in this plot is the recirculation region that is confined in the external surface. Similar behavior was found by Wick (1953) for continuum sonic flows with abrupt changes on the cross-section area. It is important to remark that this recirculation is a stable phenomenon after the flow reaches the steady state, due to the constant boundary conditions employed in the present simulations. Careful analysis about the recirculation stability should be carried out by including periodic or nonperiodic disturbances on the boundary conditions. These disturbances may be related to pressure, temperature, velocity and so on. Meanwhile, such studies are beyond the present scope.

Finally, in an effort to emphasize points of interest related to the Mach field, Fig. 5(b) depicts the contour map for the Mach number distribution in the entire simulated domain. In this plot, the dimensionless coordinates X and Y refer to the length x and to the height y normalized by the half throat size h_t, respectively. Furthermore, the hollowed circle positioned on the divergent surface represents the inflection point location. According to this plot, it is clear that the flow is essentially subsonic in the recirculation zone and along the entire internal surface. It is also interesting to note that, in general, the subsonic layer is thinner between the throat and the inflection point. However, it becomes thicker from this point up to the nozzle lip. Similarly, the sonic region starts near to the throat, covers the internal surface, and passes very close to the nozzle lip.

In the divergent and external regions, the pattern of the Mach isolines is highly dependent on the viscous layer growth and on the heat transfer from the concave surface to the gas. As long as the convex surface slope (θ_d) at the inflection point increases there is a tendency of the viscous layer growth do not occupy the centerline vicinity. As a result, within the quasi-inviscid core, the Mach number gradient is essentially parallel to the centerline, similar to quasi-one-dimensional flows. Conversely, as θ_d decreases, the viscous layer occupies most of the divergent part, and hence the flow tends to be fully viscous. Besides the friction effects, near to the concave surface, the Mach number isolines are parallel to the surface because in this region the temperature gradients are basically in the surface direction. Based on this fact, the influence of the surface temperature and viscous effects on M can be estimated by recognizing the regions where Mach isolines are nearly parallel to the surface. Thus, since $M \propto V/\sqrt{T_T}$, the Mach value decreases in the surface direction due to friction and heating effects that decreases V and increases T_T, respectively.

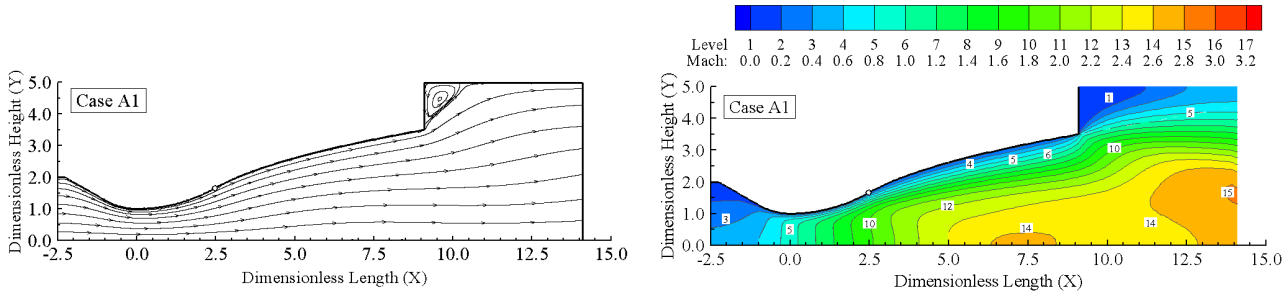

(a) (b)

Figure 5. Streamline traces (left) and Mach number (M) distribution (right) for case A1.

5.2 Pressure Field

Before proceeding with the pressure field analysis, it is desirable to gain some insight into the influence of centripetal forces related to solid surfaces with finite radius of curvature r_c. An oversimplified, but valuable analysis of such effects can be made by employing the Newton's second law along the η-direction, i.e., normal to the streamlines, as shown in Fig. 6. Therefore, by assuming a steady, two-dimensional, inviscid and continuum flow, without external force field, Eq. (8) indicates that pressure increases in the opposite direction to the curvature centre. An analogous examination can also be carried out by employing the Newton's second law along the ξ-direction, as follows in Eq. (9).

$$\frac{\partial p}{\partial \eta} = -\rho \frac{V^2}{r_c} \tag{8}$$

$$\frac{\partial p}{\partial \xi} = -\rho V \frac{\partial V}{\partial \xi} \tag{9}$$

Based on these equations (Munson *et al.*, 2002) and on the surface temperature effect, pressure and temperature

gradient directions are depicted in Fig. 6 at the vicinity of the convex and concave internal surfaces. This simplified scheme does not take into account for the combination between pressure, temperature and viscous effects. The present idea is just to elucidate the influence of each physical mechanism separately. As noted in Fig. 6, near to the surfaces the pressure gradient is composed by two components. The first component acts tangent to the streamline direction while the second component acts perpendicular to the streamline direction. In this context, an estimative of the most significant component – tangential (∇p_ξ) or normal (∇p_η) – can be made by analyzing the ratio between Eqs. (8) and (9). The result is expressed as

$$\frac{\partial p/\partial \xi}{\partial p/\partial \eta} = \frac{r_c}{V}\frac{\partial V}{\partial \xi} \tag{10}$$

For the micronozzles investigated in this work, Eq. (10) reveals essentially that the tangential component of the pressure gradient overcomes the perpendicular component in the most of the flow. It occurs because towards the surface direction, even with a finite r_c value, follows that $V \rightarrow 0$ due to the viscous effects present in the real flow. In the opposite direction, the flow speed increases to a finite value. However, for the present geometry the streamlines become straight and hence $r_c \rightarrow \infty$. In addition, the term $\partial V/\partial \xi$ is small, but finite, near to and far from the surfaces, and it does not perform significant influence on the current discussion. It is important to keep in mind that the normal component of the pressure gradient is not zero, it is just smaller than the tangential one.

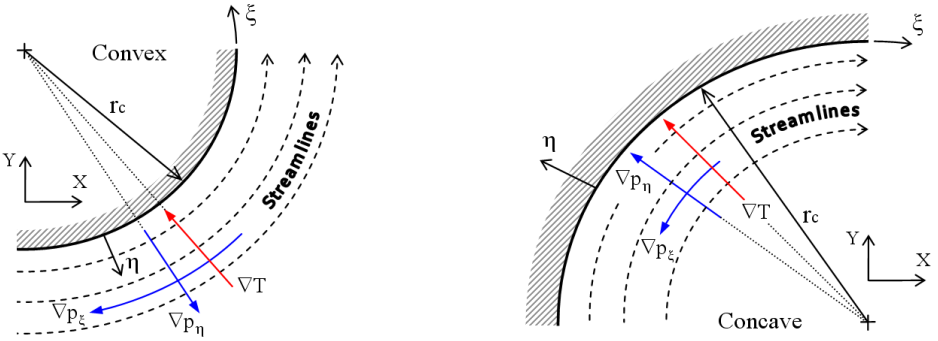

Figure 6. Schematic view of pressure and temperature gradients near the convex and concave surfaces.

For the same sections investigated previously, the influence of changing the radius of curvature on the pressure profiles is exhibited in Fig. 7. In these plots, pressure p is normalized by the inlet static pressure p_{in}. As noted in Fig. 7, pressure decreases in the downstream direction because of the gas expansion. For the divergent cross-sections located between the throat and the inflection point x-coordinate, the profiles presented a slight decreasing of the pressure ratio p/p_{in} in the surface direction. Based on the scheme introduced in Fig.6, such a pressure drop is related to the fact that, due to the streamline curvature, pressure gradients arise in the opposite direction to the curvature centre. This pressure difference is caused by the centripetal acceleration. As the flow reaches the concave surface vicinity, the centripetal effects promote a pressure increasing towards the surface direction since the curvature direction changes. In this connection, the pressure ratio tends to increase near to the surface between the inflection point x-coordinate and the exit section. For this reason, the profiles are basically uniform at the exit section.

In attempting to bring out the essential features of the pressure distribution in the micronozzles, Fig. 9(a) illustrates the pressure ratio contour map for the case A1. However, before discussing these maps in detail, it proves worthwhile to

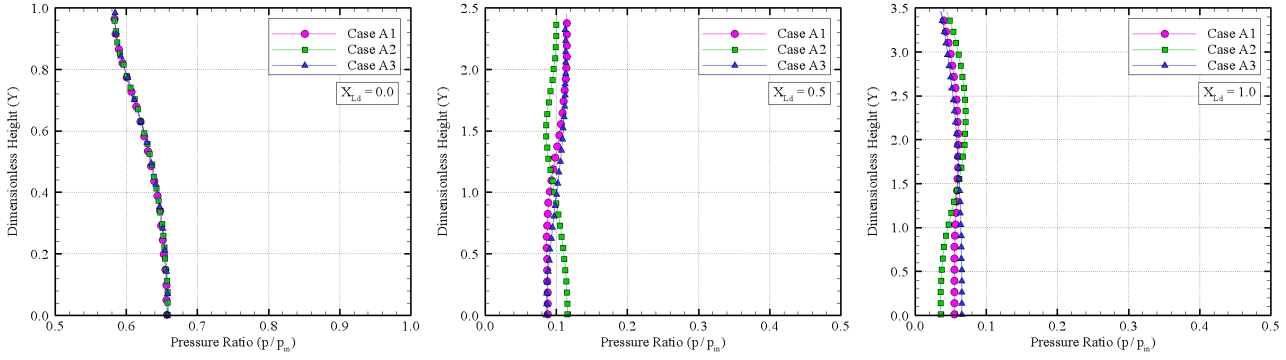

Figure 7. Pressure ratio (p/p_{in}) profiles along the micronozzle for group A cases.

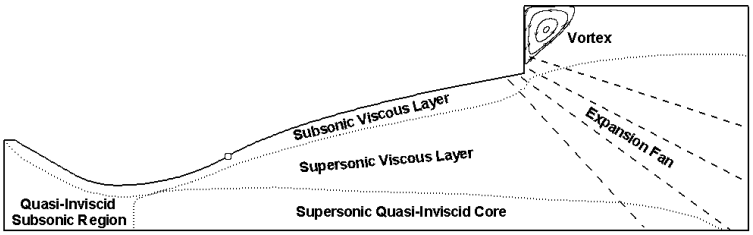

Figure 8. Qualitative flow structure observed in the current simulations.

point out the main physical mechanisms and flow aspects present in the investigated micronozzles. In this fashion, Fig. 8 summarizes qualitatively the flow structure in terms of sub- and supersonic regimes that can be classified as quasi-inviscid or viscous regions. As indicated, for the convergent part and far from the surface, the flow is essentially inviscid because of the small velocity gradients. The subsonic viscous layer established at the internal surface leading edge covers the whole micronozzle surface and extends until the external region. Slightly downstream to the throat, the flow becomes supersonic in the most micronozzle divergent part. Depending on the viscous layer growth, the supersonic flow may describe a quasi-inviscid and quasi-one-dimensional behavior along the centerline vicinity. In addition, the expansion fan developed at the nozzle lip as well as the vortex confined within the external subsonic region are highlighted.

Having an overall qualitative picture of the present micronozzle flow structure, the attention is turned to Fig. 9(a). At solid surfaces, the fluid velocity must be zero in the normal surface direction. This ensures that no mass flux occurs through such surfaces. In this context, within the whole micronozzle, the streamlines must deflect appropriately in order to become parallel to the internal surface and centerline. In such a deflection, the macroscopic flow acquires velocity in the y direction, i.e., $v \neq 0$. As a consequence of the micronozzle geometries, in general, the convergent and concave parts should present $\partial v/\partial y \leq 0$ while the convex part should present $\partial v/\partial y \geq 0$. Obviously, these velocity gradients are locally related to the appropriate pressure gradients. As discussed earlier, near to the internal surface and centerline, the tangential component of the pressure gradient overcomes the component that is perpendicular to the streamlines. As a result, the streamlines and pressure isolines tend to be perpendicular to each other in the vicinity of such boundaries. However, as long as the surface temperature effects become significant, somewhere between the concave surface and the centerline, pressure isolines tend to align parallel to the surface. Similar effects were previously found in the Mach pattern. It should also be remarked that the major pressure changes occur between the inlet and the vicinity of the inflection point.

Having a clear qualitative picture of the flow structure inside the micronozzles, particular attention is now paid to the supersonic flow around the nozzle lip. For the isentropic case, the two-dimensional continuum approach describes expansion waves in terms of the Prandtl-Meyer fan. However, because of the high rarefied nature of the present flow, the fan structure differs substantially from the ideal case, e.g., the expansion waves are not exactly attached at the sharp corner, and they perform a diffuse fashion as long as the lip distance increases. This former consequence is the responsible mechanism that promotes the merging between the recirculation region and the expansion waves. Finally, after the last expansion wave the pressure level tends to match the pre-defined back pressure p_b value. Hence, for the present account, the pressure ratio p/p_{in} may increase again downstream the expansion fan.

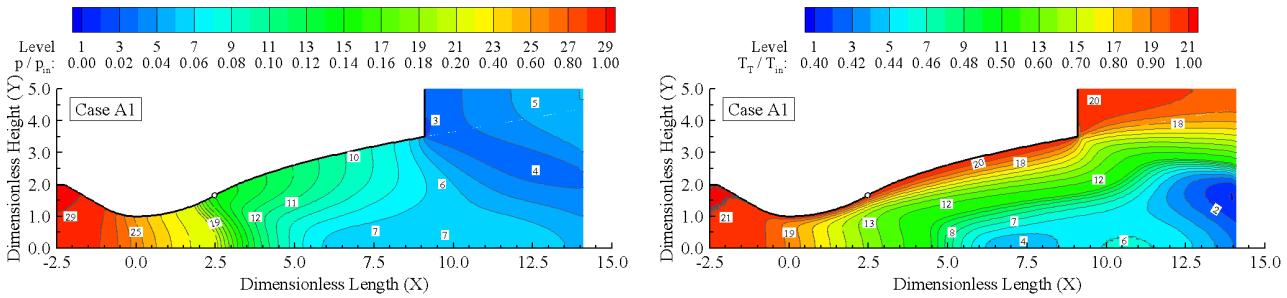

(a) (b)

Figure 9. Pressure ratio (p/p_{in}) (left) and translational temperature (T_T/T_{in}) (right) distributions for case A1.

5.3 Temperature Field

In the expansion process of a compressible flow in micronozzles, the gas temperature and density decrease while the macroscopic stream velocity increases. This behavior is assigned to conversion of the thermal energy to the macroscopic

kinetic energy. The thermal energy is related to the molecular excitation – translation, rotation, vibration, electronic, etc – and the kinetic energy is associated to the stream velocity. The opposite physical mechanism is found in shock wave problems. Across shock waves, the high kinetic energy present in the supersonic flow is rapidly converted to the thermal energy, and hence temperature and pressure should increase while the velocity decreases.

The above mentioned thermal-kinetic energy exchange is performed by successive intermolecular interactions. Therefore, a relaxation process between translational and internal modes takes place in order to lead each mode towards the equilibrium state. Thermodynamic equilibrium occurs when complete energy equipartition between translational and internal modes is achived. In this connection, the thermodynamic temperature is defined when the temperatures based on each energy mode, i.e., translational, rotational, vibrational and electronic temperatures, are equal to each other. However, the relaxation time – commonly expressed in terms of the relaxation collision number Z – differs from one mode to another. Thus, thermal nonequilibrium arises if the local collision frequency is not sufficient to return the molecules to the total statistical equilibrium. In this context, for a gas in thermodynamic nonequilibrium, an overall temperature T_O may be defined as the weighted mean of the translation and internal temperatures (Bird, 1994), as following.

$$T_O = \frac{\zeta_T T_T + \zeta_R T_R + \zeta_V T_V}{\zeta_T + \zeta_V + \zeta_R} \tag{11}$$

In this expression T and ζ stand to temperature and degree of freedoms, respectively, and the subscripts T, R and V represent the translational, vibrational and rotational modes, respectively. Evidently, ζ_T is always equal to three while the remaining excited internal degrees of freedom may vary according to the thermal state of the gas.

The effects of geometric changes on the translational temperature profiles for the same cross-sections investigated in the previous subsections are displayed in Fig. 10. By considering that the temperatures related to the internal modes present similar behavior, for cases A1, B1 and C1, then such temperatures are shown in Fig. 11 only for case A1. In the following plots, translational temperature T_T, rotational temperature T_R, vibrational temperature T_V and overall temperature T_O are normalized by the inlet thermodynamic temperature T_{in}.

By examining first Fig. 10, it is observed that the translational temperature T_T decreases in the downstream direction due to the expansion process explained in the beginning of the present subsection. Moreover, at $X_{Ld} = 0.0$, it is clear that near to the surface the translational temperature tends to the surface temperature T_w. This is an indication that at the surface vicinity the gas is in thermal equilibrium. However, for sections downstream to the throat, the translational temperature near to the surface is slightly smaller than T_w. This departure, called as temperature jump, becomes more significant in the exit section, particularly at the nozzle lip. It occurs because as the gas expands the density is reduced and, consequently, the mean free path increases and the collision frequency decreases along the downstream direction. Near to the surface, the reduction in the collision frequency promotes a local thermal nonequilibrium because molecules that interact with the surface do not perform sufficient collisions to reach a state of complete relaxation. At the lip, due to the abrupt increasing of the cross-section area, the gas expands rapidly and then the temperature jump increases substantially.

Analogous to that applied to the Mach number profiles, an examination can be made here for the temperature field. In this context, the ratio between the Y range, where the distribution of the translational temperature ratio T_T/T_{in} is nonuniform, to the total Y range of the same profile, is an indication of the thermal layer. Similarly the viscous layer, the profiles show that the aforementioned ratio increases along the downstream direction. It means that the thermal layer thickness increases and basically occupies the most section at $X_{Ld} = 1.0$. This behavior is mainly assigned to two different mechanisms, namely, the viscous dissipation and the heat transfer from the surface. Due to shear stress effects, viscous dissipation converts irreversibly the kinetic (mechanical) energy into thermal energy, i.e., such dissipation promotes a temperature rise. Evidently, this mechanism becomes more intense towards the surface, where there are strong viscous effects as well as large velocity gradients. On the other hand, with the gas expansion, the difference between the

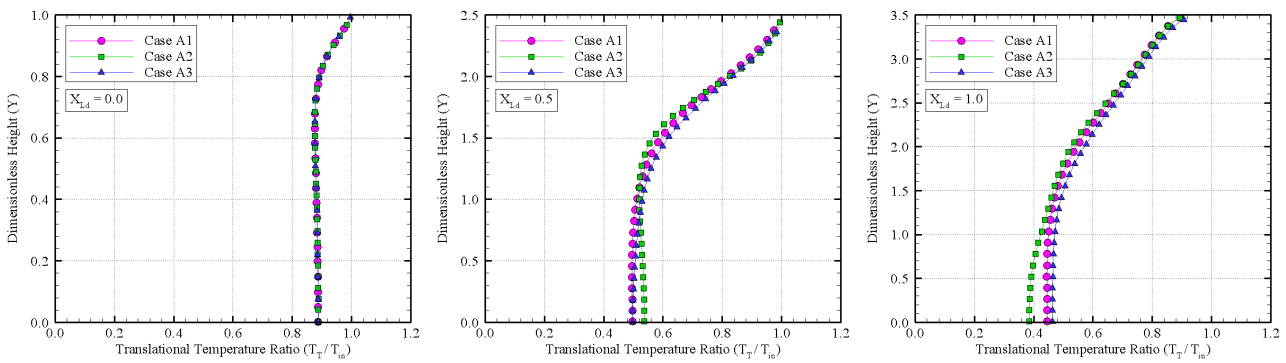

Figure 10. Translational temperature ratio (T_T/T_{in}) profiles along the micronozzle for group A cases.

surface and translational temperatures increases. Therefore, the heat transfer from the surface to the gas should become more expressive and, consequently, the temperature rise reaches larger distances.

At this point, the idea is to investigate how the translational and internal – rotational and vibrational – temperatures depart from each other along the micronozzle. This analysis should provide an clear indication of the thermal nonequilibrium degree in the gas flow. In this fashion, Fig. 11 shows normalized profiles of the translational, internal and overall temperatures for case A1.

By focusing on Fig. 11, it can be recognized that the thermodynamic nonequilibrium takes place in the entire divergent part, as showed by the lack of equilibrium between the translational and internal temperatures. In this context, it should be mentioned that the overall temperature T_O, defined by Eq. (11), is equivalent to the thermodynamic temperature only under equilibrium conditions.

In the temperature profiles, it is clear that vibrational temperature is quite larger than the other temperatures. In the same sense, the rotational temperature is slightly larger than the translational temperature. As noted, the overall temperature ratio is essentially equal to the mean value of the translational and rotational temperatures. Based on Eq. (11), it can be conclude that, on average, the excited vibrational degrees of freedom ζ_V tend to zero. In this circumstance, $T_V \geq T_R \geq T_T$ is assigned to the fact that translational and internal modes have different relaxation collision numbers, namely, $Z_V \geq Z_R \geq Z_T$. In other words, it is necessary a larger number of collisions to excite molecules vibrationally from a lower to an upper state and vice-versa, as compared to rotational mode. For this reason, T_V/T_{in} is seen to decrease much more slowly than T_R/T_{in}. Similar comparison is also valid between rotational and translational modes.

Still referring to Fig. 11, it is important to point out that the statistical fluctuations observed in the vibrational temperature profiles are assigned to the fact that the vibrational energy level is described herein by a quantum (discrete) model. Conversely, the translational and rotational modes are based on continuum spectrums of energy. Moreover, for $X_{Ld} = 1.0$, Fig. 11 revels clear differences between the temperatures at the surface ($Y = 3.5$). It confirms the aforementioned reason for the notable temperature jump at the nozzle lip. At this point, it proves worthwhile to mention that a translation nonequilibrium may be found when the local thermal velocity distribution depart from an isotropic fashion. In this condition, there exist a preferential direction for the thermal motion. However, results for the translational nonequilibrium are not shown in the present work.

Proceeding in a manner analogous to the early primary properties, it is important to demonstrate the contour map for the translational temperature ratio in the entire computational domain. In this sense, Fig. 9(b) illustrates how the temperature patterns changes along the micronozzle. According to this figure, it is noted that between the inlet and throat sections the temperature changes are similar to those in an one-dimensional fashion. This behavior occurs because upstream to the throat the difference between the surface and translational temperatures $(T_w - T_T)$ is small. Thus, the heat flux from the surface does not perform significant influence on the gas temperature. However, due to the expansion process, as the translational temperature decreases, the heat transfer influence plays the main role near to the surface. As a consequence, along the divergent part of the micronozzle, the translational temperature isolines tend to become parallel to the surface. In contrast, near to the centerline, where the heat flux from the divergent surface is less intense, the temperature changes are essentially due to the expansion process.

As pointed out in the discussion of the Mach number contour maps, near to the surface, the subsonic region becomes thick downstream to the inflection point. Similarly, in comparison to the convex surface, along the concave surface there is a thick layer that holds a high translational temperature value. Nevertheless, as showed in Fig. 6, the combination of pressure and temperature gradients takes place in different manners near to the convex and concave surfaces. Thus, since pressure is proportional to temperature, in the convex surface the pressure and temperature gradients tend to neutralize each other, while in the concave surface both pressure and temperature gradients act towards the same direction. For this reason, there is a thick layer with high temperature near to the concave surface. Consequently, this mechanism is

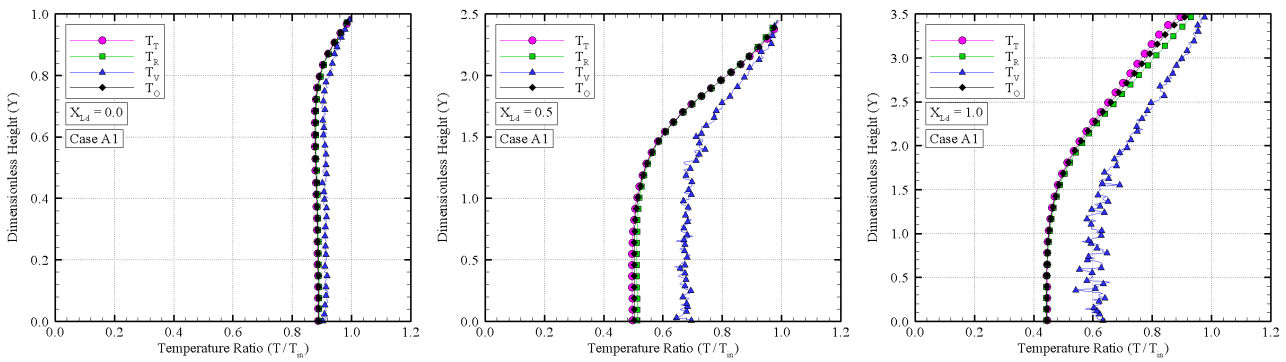

Figure 11. Temperature ratio (T/T_{in}) profiles along the micronozzle for case A1.

responsible for the thick subsonic layer previously mentioned.

By turning the attention to the external flow, $Y \approx 3.5$, it is observed that the distribution of the translational temperature follows that in the internal pattern. On the other hand, near to the centerline, the temperature gradient is basically parallel to the X-axis. It is an indication that the heat flux from the surface performs a minor impact in this part of the flow. Moreover, because of the aforementioned combination between pressure and temperature gradients, the concave surface is the main responsible for the external gas heating.

6. CONCLUDING REMARKS

In the present investigation, a rarefied flow in a rectangular cross-section convergent-divergent micronozzle array has been investigated by using the Direct Simulation Monte Carlo (DSMC) method. By considering a convex-concave divergent surface, the influence of different divergent shapes on the flowfield structure was explored by changing the radius of curvature at the inflection point.

The computational results pointed out a small impact in the primary properties – velocity, pressure and temperature – due to variations on the curvature of the divergent surface. Due to the strong viscous effects present in the micronozzle, the profiles showed a subsonic condition at the throat section. Near to the curved surfaces, centripetal effects promote different combinations between pressure and temperature gradients. As a result, the subsonic layer is thin along the convex surface and becomes thick along the concave surface. In addition, the geometric symmetry assumptions employed in the present micronozzle array resulted in a recirculation region in the external flow.

The simulations also showed that thermodynamic nonequilibrium takes place in the entire divergent flow. However, because of the rapid expansion, the largest rarefaction degree occurs at the nozzle lip. Consequently, in this region the velocity slip, temperature jump and thermal nonequilibrium are more significant. Moreover, since surface effects are predominant in microflows, the present Mach and temperature fields demonstrate to be strongly related to the heat flux from the convex surface.

In addition to the present geometries, calculations with surface discontinuities ($\alpha \neq 1.0$) might also be performed. Such investigations can provide further insight into the surface influence on the micronozzle gas flows.

7. ACKNOWLEDGEMENTS

The authors would like to thank the financial support provided by CNPq (Conselho Nacional de Desenvolvimento Científico e Tecnológico) under Grant No. 580249/2008-5.

8. REFERENCES

Alexeenko, A.A., Fedosov, D.A., Gimelshein, S.F., Levin, D.A. and Collins, R.J., 2005. "Transient Heat Transfer and Gas Flow in a MEMS-Based Thruster". *Journal of Micromechanical and Microengineering*, Vol. 15, pp. 2069–2073.

Alexeenko, A.A., Gimenlshein, S.F., Levin, D.A. and Collins, R.J., 2002. "Numerical Modeling of Axisymmetric and Three-Dimensional Flows in MEMS Nozzles". *AIAA Journal*, Vol. 40, No. 5, pp. 897–904.

Bird, G.A., 1994. *Molecular Gas Dynamics and the Direct Simulation of Gas Flows*. Oxford University Press Inc., New York. ISBN 0198561954.

Hao, P.F., Ding, Y.T., Yao, Z.H., He, F. and Zhu, K.Q., 2005. "Size Effect on Gas Flow in Micro Nozzles". *Journal of Microeletromechanical Systems*, Vol. 15, pp. 181–194.

Horisawa, H., Sawada, F., Onodera, K. and Funaki, I., 2009. "Numerical Simulation of Micro-Nozzle and Micro-Nozzle-Array Flowfield Characteristcs". *Vacuum*, Vol. 83, pp. 52–56.

Ivanov, M.S., Markelov, G.N., Ketsdver, A.D. and Wadsworth, D.C., 1999. "Numerical Study of Cold Gas Micronozzle Flows". *AIAA Paper 99–0166*.

Konecny, G., 2004. "Small Satellites–A Tool for Earth Observation?" *International Archives of Photogrammetry Remote Sensing and Spatial Information Sciences*, Vol. 35, No. 4, pp. 580–582.

Munson, B.R., Young, D.F. and Okiishi, T.H., 2002. *Fundamentals of Fluid Mechanics*. John Wiley & Son, New York, 4th edition.

Wang, M.R. and Li, Z.X., 2004. "Numerical Simulations on Performance of MEMS-Based Nozzles at Moderate or Low Temperatures". *Microfluid and Nanofluid*, Vol. 1, pp. 62–70.

Wick, R.S., 1953. "The effect of Boundary Layer on Sonic Flow Through an Abrupt Cross-Sectional Area Change". *Journal of the Aeronautical Sciences*, Vol. 20, pp. 675–682.

Zhan, K., Chou, S.K. and Ang, S.S., 2004. "MEMS-Based Solid Propellant Microthruster Design, Simulation, Fabrication, and Testing". *Journal of Microeletromechanical Systems*, Vol. 13, No. 2, pp. 165–175.

9. Responsibility notice

The authors are the only responsible for the printed material included in this paper